The Astrophysical Journal, 863:37 (9pp), 2018 August 10 https://doi.org/10.3847/1538-4357/aacf05

A New Interpretation of the Mass–Temperature Relation and Mass Calibration of Galaxy Clusters Based on the Fundamental Plane

Yutaka Fujita[1], Keiichi Umetsu[2], Stefano Ettori[3,4], Elena Rasia[5], Nobuhiro Okabe[6], and Massimo Meneghetti[3,4]
[1] Department of Earth and Space Science, Graduate School of Science, Osaka University, Toyonaka, Osaka 560-0043, Japan; fujita@astro-osaka.jp
[2] Institute of Astronomy and Astrophysics, Academia Sinica, P.O. Box 23-141, Taipei 10617, Taiwan
[3] INAF, Osservatorio di Astrofisica e Scienza dello Spazio, via Pietro Gobetti 93/3, I-40129 Bologna, Italy
[4] INFN, Sezione di Bologna, viale Berti Pichat 6/2, I-40127 Bologna, Italy
[5] INAF, Osservatorio Astronomico di Trieste, via Tiepolo 11, I-34131, Trieste, Italy
[6] Department of Physical Science, Hiroshima University, 1-3-1 Kagamiyama, Higashi-Hiroshima, Hiroshima 739-8526, Japan
Received 2018 April 10; revised 2018 June 14; accepted 2018 June 22; published 2018 August 8

Abstract

Observations and numerical simulations have shown that the relation between the mass scaled with the critical density of the universe and the X-ray temperature of galaxy clusters is approximately represented by $M_\Delta \propto T_X^{3/2}$ (e.g., $\Delta = 500$). This relation is often interpreted as evidence that clusters are in virial equilibrium. However, the recently discovered fundamental plane (FP) of clusters indicates that the temperature of clusters primarily depends on a combination of the characteristic mass M_s and radius r_s of the Navarro–Frenk–White profile rather than M_Δ. Moreover, the angle of the FP revealed that clusters are not in virial equilibrium because of continuous mass accretion from the surrounding matter. By considering both the FP and the mass dependence of the cluster concentration parameter, we show that this paradox can be solved and the relation $M_\Delta \propto T_X^{3/2}$ actually reflects the central structure of clusters. We also find that the intrinsic scatter in the halo concentration–mass relation can largely account for the spread of clusters on the FP. We also show that X-ray data alone form the FP and the angle and the position are consistent with those of the FP constructed from gravitational lensing data. We demonstrate that a possible shift between the two FPs can be used to calibrate cluster masses obtained via X-ray observations.

Key words: cosmology: theory – dark matter – galaxies: clusters: general – large-scale structure of universe

1. Introduction

Clusters of galaxies are the most massive objects in the universe. Because of their large scale, they have been expected to reflect the properties of the background universe and have been used to study cosmological parameters such as the amount of matter and dark energy, and to study the growth of large-scale structures. In particular, the mass function is one of the most powerful tools for that purpose (e.g., Bahcall & Cen 1993; Eke et al. 1996; Reiprich & Böhringer 2002; Vikhlinin et al. 2009). The cluster masses have been measured via X-ray or gravitational lensing observations. However, different measurements may be affected by different biases, which makes it complicated to be compared with the mass function from numerical simulations. To correct those biases, statistical approaches have been considered useful. In particular, scaling relations for a large number of clusters have been used as an efficient tool to estimate the biases. The relation between the mass and the X-ray temperature of the intracluster medium (ICM) or T_X is a representative one. For this relation, previous studies have adopted M_Δ or the mass enclosed within a sphere of radius r_Δ, within which the mean overdensity equals Δ times the critical density of the universe ρ_c. The critical density depends on redshift z as in $\rho_c(z) \propto E(z)^2$, where $E(z)$ is the Hubble constant at z normalized by the current value H_0. The values of $\Delta = 200$ and 500 have often been used. Observations and numerical simulations have shown that the relation is approximately represented by $M_\Delta \propto T_X^{3/2}$ for clusters (Bryan & Norman 1998; Ettori et al. 2002; Sun et al. 2009; Lieu et al. 2016; Truong et al. 2018).

This relation has often been explained as follows. Assuming that the representative density of clusters is $\rho_\Delta \equiv \Delta\rho_c(z) \propto \Delta E(z)^2$, the density does not depend on the mass at a given redshift. If a cluster is isolated and well-relaxed or "virialized" inside r_Δ, it is represented by a sphere of the radius r_Δ, which is close to isothermal. In this case, the mass is given by $M_\Delta = 4\pi\rho_\Delta r_\Delta^3/3$ and the temperature is given by $T_X \propto M_\Delta/r_\Delta \propto \rho_\Delta r_\Delta^2 \propto \Delta E(z)^2 r_\Delta^3$. From these relations, the mass–temperature relation can be represented by

$$M_\Delta \propto T_X^{3/2}\Delta^{-1/2}E(z)^{-1} \tag{1}$$

(e.g., Kaiser 1986; Bryan & Norman 1998; Borgani & Kravtsov 2011; Planelles et al. 2015), which is generally consistent with observations and simulations.

However, this conventional interpretation may appear to be at odds with a concept that came from recent numerical simulations. According to N-body simulations, the density profile of dark matter halos of galaxy clusters is not the isothermal profile ($\propto r^{-2}$) but can be represented by the Navarro–Frenk–White (NFW, hereafter) density profile:

$$\rho_{\rm DM}(r) = \frac{\delta_c\rho_c}{(r/r_s)(1 + r/r_s)^2}, \tag{2}$$

where r is the clustercentric distance, and r_s is the characteristic or scale radius (Navarro et al. 1997). The normalization of the profile is given by δ_c. We define the mass inside r_s as M_s. The ratio

$$c_\Delta = r_\Delta/r_s \tag{3}$$

is called the concentration parameter and $c_\Delta > 1$ for $\Delta = 200$ and 500 for clusters. The "inside-out" formation scenario of galaxy clusters has been proposed based on the results of the N-body simulations (Salvador-Solé et al. 1998; Fujita & Takahara 1999; Bullock et al. 2001; Wechsler et al. 2002;

Table 1
Plane Parameters

Sample	a	b	c	ϕ (degree)	θ (degree)	r_{s0} (kpc)	M_{s0} (10^{14} $M_\odot$)	T_{X0} (keV)
CLASH (CFP)	$0.76^{+0.03}_{-0.05}$	$-0.56^{+0.02}_{-0.02}$	$0.32^{+0.10}_{-0.09}$	−37	71	570	3.8	8.2
SSol[a] ($n=-2$)	0.74	−0.56	0.37	−37	68	⋯	⋯	⋯
SSol[a] ($n=-2.5$)	0.76	−0.54	0.38	−35	68	⋯	⋯	⋯
Virial	0.58	−0.58	0.58	−45	55	⋯	⋯	⋯
MUSIC	0.69	−0.57	0.44	−40	64	414	1.4	3.7
X-ray (XFP)[b]	$0.71^{+0.06}_{-0.10}$	$-0.53^{+0.02}_{-0.01}$	$0.46^{+0.13}_{-0.11}$	−37	63	443	2.2	7.3
X-ray (CC)[c]	$0.72^{+0.04}_{-0.09}$	$-0.52^{+0.02}_{-0.01}$	$0.45^{+0.12}_{-0.05}$	−36	63	529	2.7	7.1
X-ray (ICC+NCC)[d]	$0.69^{+0.10}_{-0.07}$	$-0.53^{+0.03}_{-0.02}$	$0.49^{+0.10}_{-0.23}$	−37	61	392	1.9	7.5

Notes. The vector (a, b, c) is the plane normal P_3. θ is the angle between P_3 and the $\log T_X$ axis, and ϕ is the azimuthal angle around the $\log T_X$ axis. The parameters (r_{s0}, M_{s0}, T_{X0}) represent the (logarithmic) sample means of (r_s, M_s, T_X).
[a] Similarity solution (Equation (4)).
[b] Full X-ray sample of 44 clusters.
[c] X-ray subsample of 18 cool-core (CC) clusters.
[d] X-ray subsample of 7 intermediate (ICC) and 19 non-cool-core (NCC) clusters.

Zhao et al. 2003). In this scenario, the inner region ($r \lesssim r_s$) forms rapidly, and only successively the outer region ($r \gtrsim r_s$) slowly grows through matter accretion. The inner structure at $r \lesssim r_s$ established during the fast-growing phase is well conserved in the latter slow-growing phase. The cluster formation time can be defined as the shift-time from the fast-growing phase to the slow-growing phase. Clusters that formed earlier tend to have higher characteristic density $\rho_s \equiv 3M_s/(4\pi r_s^3)$ (Navarro et al. 1997; Zhao et al. 2009; Ludlow et al. 2013; Correa et al. 2015). Contrary to ρ_Δ, this representative density ρ_s is not constant among clusters at a given z. Moreover, the inside-out scenario indicates that clusters are not well-relaxed in the entire region within r_Δ. These suggest that the conventional virial interpretation of the relation $M_\Delta \propto T_X^{3/2}$ might need to be reconsidered.

In this study, we propose a new interpretation of the relation $M_\Delta \propto T_X^{3/2}$, which is consistent with the inside-out scenario. This interpretation is based on the newly discovered fundamental plane (FP) of clusters (Fujita et al. 2018, hereafter Paper I) and the mass dependence of the concentration parameter c_Δ. We also investigate the FP constructed from X-ray data alone in order to endorse studies of scaling relations based on X-ray data. The rest of the paper is organized as follows. In Section 2, we summarize the properties of the FP. In Section 3, we show that the mass–temperature relation can be explained by considering both the FP and the cluster concentration parameter, c_Δ. In Section 4, we show that the FP formed by X-ray data alone is consistent with the FP we found in Paper I. In Section 5, we propose a new calibration method of cluster mass using the FP. Finally, in Section 6 we summarize our main results. We use cosmological parameters $\Omega_0 = 0.27$, $\lambda = 0.73$, and $h = 0.7$ throughout the paper.

2. The FP of Galaxy Clusters

In Paper I, we studied 20 massive clusters from the Cluster Lensing And Supernova survey with Hubble (CLASH) observational data set (Postman et al. 2012; Donahue et al. 2014; Meneghetti et al. 2014; Umetsu et al. 2016). For these clusters, r_s and M_s were derived by gravitational lensing, and the X-ray temperatures T_X were obtained by *Chandra* observations. We found that the clusters form a two-parameter family and thus they are distributed on a plane in the space of ($\log r_s$, $\log M_s$, $\log T_X$), which is described by $a \log r_s + b \log M_s + c \log T_X = \text{const.}$, with $a = 0.76^{+0.03}_{-0.05}$, $b = -0.56^{+0.02}_{-0.02}$, and $c = 0.32^{+0.10}_{-0.09}$ (Table 1). The plane normal is represented by $P_3 = (a, b, c)$, and the dispersion around the plane is $0.045^{+0.008}_{-0.007}$ dex. The plane normal and the errors are obtained through a principal component analysis (PCA) and Monte-Carlo realizations. From now on, we assume that the length of the plane normal is $|P_3| = \sqrt{a^2 + b^2 + c^2} = 1$ unless noted otherwise. We showed in Paper I that numerical simulations reproduce the plane regardless of relaxation of clusters, redshifts, and gas physics such as radiative cooling and active galactic nucleus (AGN) feedback. In particular, clusters evolve within this plane and do not substantially deviate from the plane even during major mergers. This FP is consistent with the one predicted from the similarity solution for structure formation by Bertschinger (1985):

$$r_s^2 M_s^{-(n+11)/6} T_X = \text{const}, \tag{4}$$

or $T_X \propto M_s^{(n+11)/6}/r_s^2$, where n is the power spectrum index of the initial density fluctuations of the universe (Paper I). The index is $n \sim -2$ at cluster scales (Eisenstein & Hu 1998; Diemer & Kravtsov 2015). Since X-ray emissions mostly come from the inner region of clusters ($r \lesssim r_s$), T_X mostly reflects the temperature therein. Thus, it should depend on the gravitational potential that is represented by r_s and M_s, which is consistent with Equation (4). Since r_s and M_s are conserved in the slow-growing phase, it may be natural to expect that T_X is also conserved in that phase.

However, Equation (4) is different from the one expected from virial equilibrium at the formation of the inner structure or $T_X \propto M_s/r_s$ (virial expectation). If a cluster is isolated and steady, the virial theorem is given by $2K + W = 0$, where K is the kinetic and/or thermal energy and W is the gravitational energy. This should give the expression above ($T_X \propto M_s/r_s$). However, if the cluster is not isolated and is growing, the virial theorem requires a term of $d^2I/dt^2/2$, where I is the moment of inertia, and two boundary terms originating from the flux of inertia through the boundary and the pressure at the boundary (Bertschinger 1985; Shi 2016b). The peculiar relation of Equation (4) is attributed to these effects. In Paper I, we also

studied data distribution in the space of (r_{200}, M_{200}, T_X), and confirmed that the data points follow the obvious relation of $M_{200} \propto r_{200}^3$.

3. Mass–Temperature Relation

In this section, we derive the mass–temperature relation from the FP relation and the concentration parameter c_Δ.

The mass profile of a cluster is well described by the NFW formula and can be derived from Equation (2):

$$M(r) = 4\pi\delta_c \rho_c r_s^3 \left[\ln\left(1 + \frac{r}{r_s}\right) - \frac{r}{r + r_s}\right]. \quad (5)$$

From the definition of M_Δ, we obtain

$$r_\Delta = \left(\frac{3M_\Delta}{4\pi\Delta\ \rho_c(z)}\right)^{1/3}. \quad (6)$$

From Equations (5) and (6), the normalization is given by

$$\delta_c = \Delta y(c_\Delta), \quad (7)$$

where

$$y(x) \equiv \frac{1}{3}\ \frac{x^3}{\ln(1 + x) - x/(1 + x)}, \quad (8)$$

and the characteristic mass is given by

$$M_s = M_\Delta \frac{\ln 2 - 1/2}{\ln(1 + c_\Delta) - c_\Delta/(1 + c_\Delta)}. \quad (9)$$

Equations (3) and (9) show that the ratios r_s/r_Δ and M_s/M_Δ are functions of c_Δ.

Previous studies have shown that the concentration parameter c_Δ is a function of the mass M_Δ and the observed redshift z of a cluster. For example, Duffy et al. (2008) obtained an empirical relation for $\Delta = 200$ from N-body simulations:

$$c_{200}(M_{200}, z) = 6.71 \left(\frac{M_{200}}{2 \times 10^{12} h^{-1} M_\odot}\right)^{-0.091} (1 + z)^{-0.44} \quad (10)$$

for $M_{200} \sim 10^{11}$–$10^{15} h^{-1} M_\odot$ and $z < 2$ (see also Bhattacharya et al. 2013; Dutton & Macciò 2014; Meneghetti et al. 2014; Diemer & Kravtsov 2015). Correa et al. (2015) considered the mass accretion history of dark halos and proposed an analytical model based on the inside-out scenario. Their model reproduces Equation (10) and is applicable even to smaller M_{200}, larger z, and various cosmological parameters. We use their code COMMAH[7,8] to calculate $c_\Delta(M_\Delta, z)$.

For a given z and Δ, the M_Δ–T_X relation can be obtained as follows. The mass M_Δ is converted to M_s by Equation (9) and $c_\Delta(M_\Delta, z)$. The radius r_Δ is a function of M_Δ (Equation (6)), and it is converted to r_s by Equation (3) and $c_\Delta(M_\Delta, z)$. Here, we use the analytically derived FP (Equation (4)). Thus, the temperature is given by

$$T_X = T_{X0}\left(\frac{r_s}{r_{s0}}\right)^{-2}\left(\frac{M_s}{M_{s0}}\right)^{(n+11)/6}, \quad (11)$$

where (r_{s0}, M_{s0}, T_{X0}) correspond to a representative point on the FP. Since the similarity solution does not predict (r_{s0}, M_{s0}, T_{X0}), we adopt the logarithmic mean of the parameters for the MUSIC simulation sample; $r_{s0} = 414$ kpc, $M_{s0} = 1.4 \times 10^{14}\ M_\odot$, and $T_{X0} = 3.7$ keV (Table 1, see also Figure 2). The MUSIC simulation set that we consider is from non-radiative runs and includes 402 clusters at $z = 0.25$ with $M_{200} > 2 \times 10^{14}\ h^{-1}\ M_\odot$ (Paper I, see also Meneghetti et al. 2014). Assigning r_s and M_s in Equation (11), we finally obtain the M_Δ–T_X relation. Numerical simulations have shown that the c_Δ–M_Δ relation has an intrinsic scatter of $\sim$0.1 dex at $M_{200} \sim 10^{14}$–$M^{15}\ M_\odot$ (Bullock et al. 2001; Duffy et al. 2008; Ludlow et al. 2013; Meneghetti et al. 2014; Correa et al. 2015). Thus, we also calculate the M_Δ–T_X relations when c_Δ (fiducial) is replaced by $c_\Delta^U = 10^{0.1} c_\Delta$ (upper limit) or $c_\Delta^L = 10^{-0.1} c_\Delta$ (lower limit). In the cluster mass range the scatter of the relation is not particularly sensitive to the baryonic physics or to the fitting radial range. In fact, Rasia et al. (2013) found an intrinsic scatter of $\sim$0.1 dex for the relations obtained from simulations both with and without AGN feedback (Tables 1 and 2 of Rasia et al. 2013). Figure 1 shows the relation M_Δ–T_Δ for $\Delta = 500$ at $z = 0$ and 1. We adopt $n = -2$ for Figure 1(a). The slope of the lines at $1 \lesssim T_X \lesssim 7$ keV is $\alpha = 1.33$ for $z = 0$ ($E(z)M_{500} \propto T_X^\alpha$). The values are close to 3/2 or 1.5, and c_Δ^U gives smaller M_{500} than c_Δ^L. This relation holds even when $\Delta = 200$ and 2500. We emphasize that we did not use the assumption of virial equilibrium when we derive the relation. The figure also shows that the vertical dispersion of the relations should be within a factor of two. The slight difference of the obtained slope α from 1.5 may be due to some simplified assumption we made when we derived the plane angle. For example, Equation (4) is exactly correct only for the Einstein–de Sitter universe because it is based on a similarity solution. For the ΛCDM cosmology we adopted, the angle of the plane could slightly change (Bertschinger 1985; Paper I, see also Shi 2016a).

In fact, the slope of $\alpha \sim 1.5$ can be obtained if we change the plane angle only slightly. Figure 1(b) is the same as Figure 1(a) but for $n = -2.5$ in Equation (4). While the plane angle is almost the same as that for $n = -2$ (Table 1) and is consistent with the observations (see Figure 4), the slope of the lines is $\alpha = 1.53$ for $z = 0$. Thus, an imperceptible modification of the angle is enough to obtain $\alpha \sim 1.5$. We also note that the power spectrum index n is expected to be smaller at smaller scales. For example, $n \sim -2.5$ is expected at group scales ($M_{200} \sim 10^{13}\ M_\odot$; e.g., Diemer & Kravtsov 2015). This means that the M_Δ–T_X relation should become qualitatively steeper toward lower T_X.

Figure 2 shows the relation between r_s and M_s at $z = 0.25$; they are calculated using $c_{200}(M_{200}, z)$. We also plot the data points of the MUSIC simulation (Paper I). For the simulation, the scale radius r_s is obtained by fitting the total density distribution (gas+dark matter) with the NFW profile up to r_{200}. The mass M_s is then derived as the mass enclosed by a sphere of radius r_s. The figure is similar to Figure 5(a) of Paper I and it is the projection of the FP on the r_s–M_s plane. As can be seen, most of the data points are distributed inside the upper and lower limits of c_Δ. This clearly indicates that the dispersion of the c_Δ–M_Δ relation corresponds to the spread of the cluster

[7] https://bitbucket.org/astroduff/commah

[8] Although COMMAH gives only c_{200}, it can be converted to c_Δ for arbitrary Δ using the profile given by Equation (2).

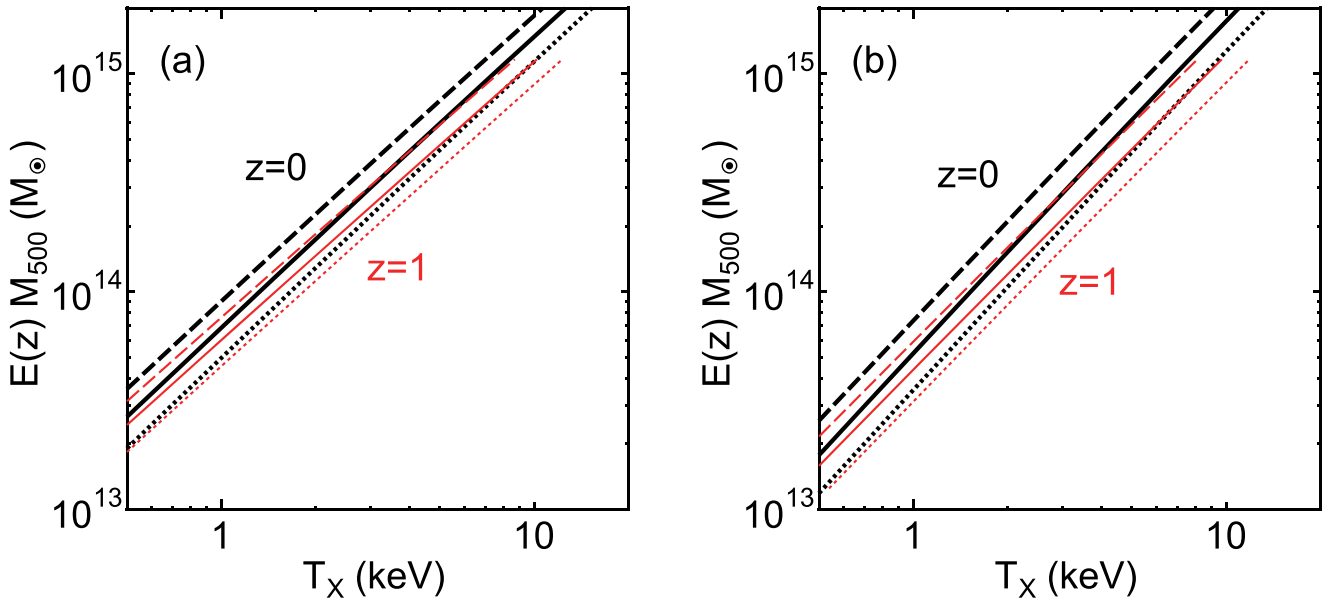

Figure 1. (a) Relation between M_Δ and T_X for $\Delta = 500$ and $n = -2$. The thick black lines and the thin red lines represent $z = 0$ and $z = 1$, respectively. The solid lines are calculated for the fiducial c_Δ. The dotted and dashed lines correspond to c_Δ^U and c_Δ^L, respectively. The slope of the relation at $1 \lesssim T_X \lesssim 7$ keV is $\alpha = 1.33$ for $z = 0$, and $\alpha = 1.28$ for $z = 1$ ($E(z)M_{500} \propto T_X^\alpha$). (b) Same as (a) but for $n = -2.5$. The slope of the relation at $1 \lesssim T_X \lesssim 7$ keV is $\alpha = 1.53$ for $z = 0$, and $\alpha = 1.45$ for $z = 1$.

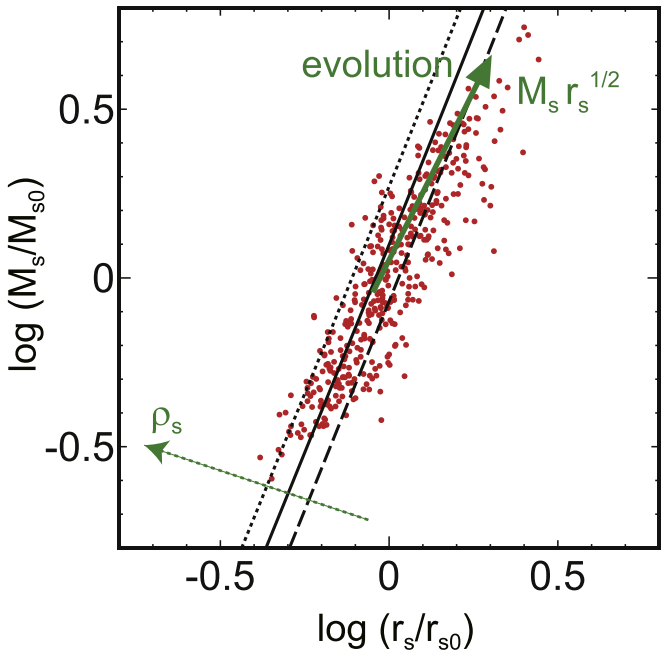

Figure 2. Relation between M_s and r_s at $z = 0.25$. The black solid line is calculated for the fiducial c_Δ. The black dotted and dashed lines are calculated for c_Δ^U and c_Δ^L, respectively. Individual clusters generally evolve in the direction of the green solid arrow to which the value $M_s r_s^{1/2}$ increases. The characteristic density ρ_s increases and the cluster formation epoch occurs earlier in the direction of the green dotted arrow. Note that the dotted green arrow is almost (but not perfectly) perpendicular to the three parallel black lines. Red dots are the data points of the MUSIC simulation at $z = 0.25$, which are the same as those in Figure 5(a) of Paper I.

distribution along the minor axis of the FP. Note that the limits along the major axis or the larger and smaller M_s limits of the MUSIC data distribution are set by the box size and the resolution of the simulation, respectively. The characteristic density ρ_s increases in the direction of the dotted green arrow. Since the three black lines are almost (but not perfectly) perpendicular to the arrow representing the direction of the ρ_s axis, the variation of c_Δ is closely related to that of ρ_s or the formation time of clusters, although it is not a precise one-to-one correspondence. Individual clusters evolve toward lower ρ_s as a whole, but the actual direction (solid green arrow) is mostly determined by the power spectrum of the initial density fluctuations of the universe, and cluster mergers temporally disturb this motion on the FP (Paper I).

4. FP in X-Rays

Since X-ray data have shown that the relation $M_\Delta \propto T_X^{3/2}$ is generally satisfied (Ettori & Fabian 1999; Neumann & Arnaud 1999; Nevalainen et al. 2000; Finoguenov et al. 2001; Xu et al. 2001; Vikhlinin et al. 2006), we expect that X-ray data alone form the FP. We will confirm this in this section.

The characteristic radius r_s and mass M_s can be derived from X-ray data, assuming that the ICM is in hydrostatic equilibrium. Using the X-ray data of 44 clusters obtained with *XMM-Newton* (Ettori et al. 2010; Table 2), we study their distribution in the space of ($\log r_s$, $\log M_s$, $\log T_X$). The average redshift of the clusters is 0.189. The logarithmic means of (r_s, M_s, T_X) for this sample are $r_{s0} = 443$ kpc, $M_{s0} = 2.2 \times 10^{14}\ M_\odot$, and $T_{X0} = 7.3$ keV (Table 1). While we adopt the values obtained through method 1 in Ettori et al. (2010), the results are not much different even if we use those obtained through method 2. In Table 2, the X-ray temperatures (T_X) and masses (M_{200}) obtained by Ettori et al. (2010) are listed as $T_{\rm XMM}$ and $M_{200,\rm XMM}$, respectively. The temperatures are the error-weighted mean of the spectral measurements in the radial range [0.15 r_{500}, min(r_{500}, $R_{\rm xsp}$)], where $R_{\rm xsp}$ is the maximum radius up to which X-ray spectra can be extracted (see Table 2 of Ettori et al. 2010). This means that $M_{200,\rm XMM}$ and c_{200} are estimated from the X-ray emission at $\leqslant r_{500}$. It has been

Table 2
Cluster X-Ray Data

Cluster	z	r_s (kpc)	c_{200}	$M_{200,\mathrm{XMM}}$ ($10^{14}\ M_\odot$)	$M_{200,\mathrm{Ch}}$ ($10^{14}\ M_\odot$)	T_{XMM} (keV)	T_{Ch} (keV)
RXCJ 0003.8+0203	0.092	143^{+36}_{-28}	$8.06^{+1.52}_{-1.30}$	1.90 ± 0.23	$2.28^{+0.28}_{-0.28}$	4.0 ± 0.3	$4.8^{+0.4}_{-0.4}$
Abell 3911	0.097	261^{+108}_{-59}	$5.59^{+1.33}_{-1.39}$	3.88 ± 0.50	$4.77^{+0.62}_{-0.63}$	5.1 ± 0.7	$6.2^{+1.0}_{-0.9}$
Abell 3827	0.098	390^{+89}_{-64}	$4.47^{+0.67}_{-0.64}$	6.61 ± 0.73	$8.37^{+0.93}_{-0.93}$	6.8 ± 0.3	$8.6^{+0.4}_{-0.4}$
RXCJ 0049.4-2931	0.108	71^{+30}_{-19}	$12.78^{+3.80}_{-3.18}$	0.94 ± 0.16	$1.10^{+0.19}_{-0.19}$	3.3 ± 0.8	$3.8^{+1.0}_{-1.0}$
Abell 2034	0.113	979^{+7}_{-317}	$2.46^{+0.81}_{-0.06}$	17.64 ± 2.17	$22.18^{+2.76}_{-2.78}$	6.4 ± 0.9	$8.0^{+1.3}_{-1.3}$
RXCJ 1516.5-0056	0.115	563^{+0}_{-114}	$2.75^{+0.50}_{-0.06}$	4.73 ± 0.42	$5.66^{+0.51}_{-0.52}$	3.9 ± 0.6	$4.7^{+0.8}_{-0.8}$
RXCJ 2149.1-3041	0.118	251^{+41}_{-28}	$4.79^{+0.43}_{-0.49}$	2.21 ± 0.21	$2.63^{+0.26}_{-0.26}$	3.7 ± 0.3	$4.4^{+0.5}_{-0.4}$
RXCJ 1516.3+0005	0.118	185^{+67}_{-42}	$7.06^{+1.64}_{-1.54}$	2.84 ± 0.41	$3.48^{+0.51}_{-0.51}$	4.9 ± 0.2	$6.1^{+0.4}_{-0.3}$
RXCJ 1141.4-1216	0.119	496^{+60}_{-36}	$3.15^{+0.19}_{-0.24}$	4.88 ± 0.37	$5.76^{+0.45}_{-0.45}$	3.5 ± 0.5	$4.1^{+0.6}_{-0.6}$
RXCJ 1044.5-0704	0.132	286^{+23}_{-27}	$4.56^{+0.34}_{-0.25}$	2.86 ± 0.18	$3.41^{+0.22}_{-0.22}$	3.7 ± 0.3	$4.4^{+0.4}_{-0.4}$
Abell 1068	0.138	564^{+66}_{-49}	$3.02^{+0.20}_{-0.22}$	6.40 ± 0.48	$7.73^{+0.61}_{-0.60}$	4.3 ± 0.9	$5.2^{+1.2}_{-1.2}$
RXCJ 2218.6-3853	0.138	597^{+184}_{-166}	$3.16^{+0.85}_{-0.55}$	8.76 ± 1.62	$10.98^{+2.03}_{-2.05}$	6.2 ± 0.5	$7.8^{+0.7}_{-0.7}$
RXCJ 0605.8-3518	0.141	369^{+47}_{-39}	$4.10^{+0.34}_{-0.34}$	4.51 ± 0.36	$5.49^{+0.44}_{-0.44}$	4.6 ± 0.3	$5.6^{+0.4}_{-0.4}$
RXCJ 0020.7-2542	0.142	473^{+245}_{-154}	$4.17^{+1.41}_{-1.07}$	10.03 ± 2.67	$12.39^{+3.31}_{-3.33}$	5.5 ± 1.2	$6.8^{+1.7}_{-1.7}$
Abell 1413	0.143	287^{+23}_{-32}	$5.83^{+0.57}_{-0.35}$	6.12 ± 0.32	$7.68^{+0.44}_{-0.43}$	6.3 ± 1.1	$7.9^{+1.5}_{-1.4}$
RXCJ 2048.1-1750	0.147	742^{+80}_{-370}	$2.23^{+1.63}_{-0.21}$	5.96 ± 1.12	$7.34^{+1.38}_{-1.39}$	5.2 ± 0.4	$6.4^{+0.5}_{-0.5}$
RXCJ 0547.6-3152	0.148	443^{+253}_{-71}	$4.10^{+0.59}_{-1.17}$	7.89 ± 1.51	$9.90^{+1.89}_{-1.91}$	6.3 ± 0.3	$7.9^{+0.5}_{-0.5}$
Abell 2204	0.152	816^{+137}_{-0}	$2.81^{+0.02}_{-0.28}$	15.93 ± 1.20	$20.48^{+1.59}_{-1.57}$	8.0 ± 1.0	$10.3^{+1.4}_{-1.4}$
RXCJ 0958.3-1103	0.153	872^{+260}_{-183}	$2.39^{+0.42}_{-0.39}$	11.94 ± 2.02	$14.87^{+2.54}_{-2.55}$	5.8 ± 1.0	$7.3^{+1.5}_{-1.4}$
RXCJ 2234.5-3744	0.153	506^{+261}_{-220}	$4.28^{+2.31}_{-1.16}$	13.42 ± 4.15	$17.19^{+5.30}_{-5.34}$	7.7 ± 1.0	$9.9^{+1.4}_{-1.4}$
RXCJ 2014.8-2430	0.161	462^{+59}_{-25}	$3.86^{+0.15}_{-0.30}$	7.56 ± 0.53	$9.52^{+0.68}_{-0.68}$	6.5 ± 0.6	$8.2^{+0.8}_{-0.8}$
RXCJ 0645.4-5413	0.167	380^{+135}_{-89}	$4.58^{+1.06}_{-0.96}$	7.08 ± 1.12	$9.14^{+1.45}_{-1.45}$	8.4 ± 0.3	$10.8^{+0.5}_{-0.5}$
Abell 2218	0.176	243^{+95}_{-79}	$6.26^{+2.46}_{-1.48}$	4.76 ± 0.74	$5.98^{+0.93}_{-0.94}$	6.3 ± 0.6	$7.9^{+0.8}_{-0.8}$
Abell 1689	0.183	211^{+22}_{-19}	$8.31^{+0.64}_{-0.63}$	7.36 ± 0.44	$9.52^{+0.59}_{-0.58}$	8.5 ± 0.8	$11.0^{+1.2}_{-1.2}$
Abell 383	0.187	435^{+95}_{-0}	$3.40^{+0.03}_{-0.42}$	4.43 ± 0.37	$5.33^{+0.45}_{-0.46}$	4.1 ± 0.3	$4.9^{+0.4}_{-0.4}$
Abell 209	0.206	604^{+272}_{-133}	$3.03^{+0.67}_{-0.77}$	8.60 ± 1.23	$10.80^{+1.57}_{-1.57}$	6.4 ± 1.2	$8.1^{+1.7}_{-1.6}$
Abell 963	0.206	377^{+107}_{-83}	$4.35^{+0.94}_{-0.76}$	6.17 ± 0.83	$7.74^{+1.04}_{-1.05}$	6.2 ± 0.4	$7.8^{+0.6}_{-0.6}$
Abell 773	0.217	605^{+408}_{-233}	$3.27^{+1.49}_{-1.05}$	10.94 ± 3.12	$13.92^{+3.96}_{-3.98}$	7.3 ± 1.0	$9.3^{+1.4}_{-1.4}$
Abell 1763	0.223	192^{+194}_{-49}	$7.50^{+2.30}_{-3.42}$	4.25 ± 0.74	$5.39^{+0.94}_{-0.94}$	6.8 ± 0.4	$8.7^{+0.5}_{-0.5}$
Abell 2390	0.228	1258^{+0}_{-95}	$2.06^{+0.12}_{-0.04}$	24.71 ± 1.16	$32.55^{+1.89}_{-1.89}$	10.4 ± 2.8	$13.8^{+4.1}_{-4.0}$
Abell 2667	0.230	993^{+0}_{-48}	$2.25^{+0.08}_{-0.02}$	15.88 ± 0.45	$20.19^{+0.72}_{-0.70}$	7.1 ± 1.0	$9.1^{+1.5}_{-1.4}$
RXCJ 2129.6+0005	0.235	418^{+68}_{-37}	$3.71^{+0.27}_{-0.38}$	5.40 ± 0.44	$6.66^{+0.55}_{-0.55}$	5.2 ± 0.5	$6.5^{+0.7}_{-0.7}$
Abell 1835	0.253	866^{+46}_{-143}	$2.64^{+0.34}_{-0.09}$	17.53 ± 1.41	$22.59^{+1.91}_{-1.88}$	8.2 ± 1.5	$10.6^{+2.1}_{-2.1}$
RXCJ 0307.0-2840	0.253	611^{+297}_{-175}	$3.15^{+0.88}_{-0.78}$	10.44 ± 2.39	$13.03^{+3.01}_{-3.01}$	6.1 ± 1.5	$7.7^{+2.1}_{-2.1}$
Abell 68	0.255	834^{+0}_{-257}	$2.65^{+0.82}_{-0.06}$	15.96 ± 1.98	$20.20^{+2.53}_{-2.55}$	6.9 ± 1.1	$8.7^{+1.6}_{-1.5}$
E 1455+2232	0.258	214^{+26}_{-22}	$6.33^{+0.53}_{-0.51}$	3.66 ± 0.29	$4.47^{+0.36}_{-0.36}$	4.7 ± 0.5	$5.7^{+0.7}_{-0.7}$
RXCJ 2337.6+0016	0.273	332^{+342}_{-154}	$4.99^{+3.52}_{-2.18}$	6.81 ± 1.91	$8.61^{+2.41}_{-2.43}$	6.7 ± 1.1	$8.5^{+1.6}_{-1.5}$
RXCJ 0303.8-7752	0.274	1115^{+14}_{-497}	$1.85^{+1.04}_{-0.09}$	13.21 ± 2.33	$16.40^{+3.27}_{-3.44}$	7.0 ± 4.1	$8.9^{+5.9}_{-5.5}$
RXCJ 0532.9-3701	0.275	278^{+170}_{-98}	$5.97^{+2.43}_{-1.82}$	6.88 ± 1.83	$8.71^{+2.33}_{-2.34}$	7.0 ± 1.6	$8.9^{+2.3}_{-2.2}$
RXCJ 0232.4-4420	0.284	1172^{+0}_{-409}	$1.80^{+0.66}_{-0.04}$	14.28 ± 1.91	$18.37^{+2.48}_{-2.49}$	8.1 ± 1.4	$10.4^{+2.0}_{-2.0}$
ZW 3146	0.291	510^{+61}_{-31}	$3.37^{+0.15}_{-0.25}$	7.79 ± 0.49	$9.85^{+0.63}_{-0.63}$	6.8 ± 0.5	$8.5^{+0.7}_{-0.7}$
RXCJ 0043.4-2037	0.292	186^{+196}_{-81}	$7.80^{+5.05}_{-3.51}$	4.70 ± 1.24	$5.79^{+1.55}_{-1.55}$	5.5 ± 1.6	$6.9^{+2.3}_{-2.2}$
RXCJ 0516.7-5430	0.295	785^{+405}_{-472}	$2.41^{+2.82}_{-0.75}$	10.44 ± 2.88	$13.02^{+3.60}_{-3.62}$	5.9 ± 1.1	$7.4^{+1.5}_{-1.4}$
RXCJ 1131.9-1955	0.307	797^{+494}_{-309}	$2.43^{+1.16}_{-0.76}$	11.31 ± 2.50	$14.06^{+3.23}_{-3.23}$	6.3 ± 2.6	$8.0^{+3.6}_{-3.5}$

Note. $M_{200,\mathrm{XMM}}$ is the mass M_{200} originally obtained with *XMM-Newton*, and $M_{200,\mathrm{Ch}}$ is the one corrected for the systematic difference of measured temperature between *Chandra* and *XMM-Newton*. T_{XMM} is the X-ray temperature originally obtained with *XMM-Newton*, and T_{Ch} is the corresponding *Chandra* temperature (Equation (12)).

indicated that the temperatures obtained with *XMM-Newton* tend to be lower than those obtained with *Chandra* (Nevalainen et al. 2010; Donahue et al. 2014; Israel et al. 2015; Schellenberger et al. 2015; Zhao et al. 2015). Since the temperatures we used for the CLASH sample have been derived with *Chandra* (Postman et al. 2012), a correction is required to compare the temperatures between the two samples. Ettori et al. (2010) used only MOS1+MOS2, with MOS2 as a value of reference. We convert T_{XMM} in Table 2 into the equivalent *Chandra* temperature T_{Ch} using the relation

$$\log \frac{T_{\mathrm{Ch}}}{\mathrm{keV}} = \frac{1}{A}\left(\log \frac{T_{\mathrm{XMM}}}{\mathrm{keV}} - B\right), \tag{12}$$

where $A = 0.909^{+0.005}_{-0.005}$ and $B = -0.017^{+0.003}_{-0.004}$ (Schellenberger et al. 2015). Hereafter, we consider T_X as the corrected

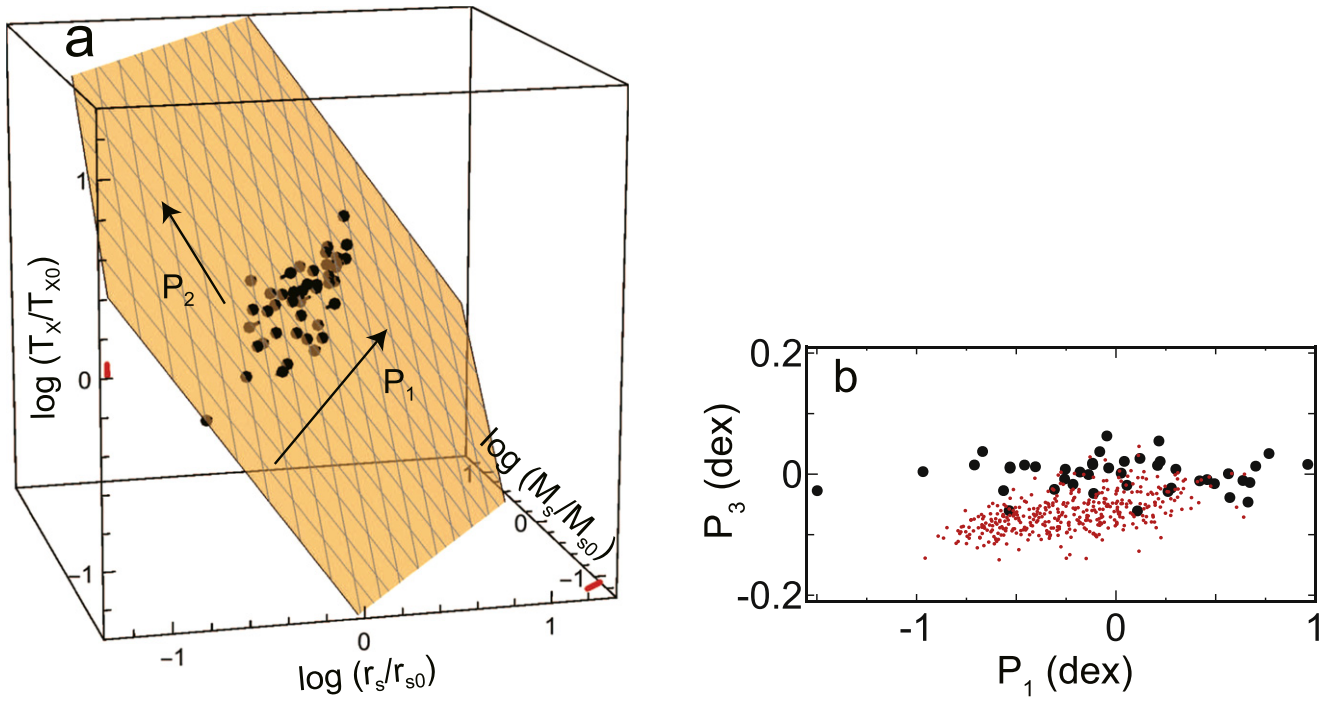

Figure 3. (a) Points (pin heads) show the distribution of the 44 X-ray clusters in the space of $(\log(r_s/r_{s0}), \log(M_s/M_{s0}), \log(T_X/T_{X0}))$, where $r_{s0} = 443$ kpc, $M_{s0} = 2.2 \times 10^{14}\,M_\odot$, and $T_{X0} = 7.3$ keV are the sample geometric averages (log means) of r_s, M_s, and T_X, respectively. The length of a pin shows the distance between the point and the obtained plane. The orange plane is translucent and grayish points are located below the plane. The arrow P_1 shows the direction on the plane in which the data are most extended, and the arrow P_2 is perpendicular to P_1 on the plane. The red bars at the corner of the $\log r_s$–$\log M_s$ plane and on the $\log T_X$ axis are typical 1σ errors of the data. (b) Cross section of the plane shown in (a). The origin is the same as (a) and P_3 is the plane normal. The large black points are the X-ray clusters shown in (a). The small red points are the MUSIC-simulated clusters projected on the P_1–P_3 plane determined for the X-ray clusters.

temperature, $T_{\rm Ch}$. Moreover, since cluster mass is estimated based on the temperature, we convert $M_{200,\rm XMM}$ in Table 2 into the equivalent *Chandra* mass $M_{200,\rm Ch}$ using the relation $M_{200,\rm Ch} = (T_{\rm Ch}/T_{\rm XMM})M_{200,\rm XMM}$ and we refer to $M_{200,\rm Ch}$ as M_{200}. The correction does not really affect the following results because we discuss the FP in the logarithmic space. We calculate M_s from M_{200} and c_{200} using Equation (9) assuming that c_{200} is anti-correlated with r_s (Figure 2 of Ettori et al. 2010).

In Figure 3(a), we show the results for the whole sample of 44 clusters; the data points have a planar distribution. The cross section of the plane is shown in Figure 3(b). In this figure, we project the simulated MUSIC clusters on the cross section of the X-ray cluster plane for comparison. The distribution of the MUSIC clusters is slightly deviated from that of the X-ray clusters. We will discuss the absolute position of the X-ray cluster plane in Section 5. We determine the direction of the X-ray cluster plane and the errors through a PCA and Monte-Carlo realizations (see Paper I). The direction on the plane in which the data are most extended is P_1, and the direction perpendicular to P_1 on the plane is P_2. The plane is described by $a \log r_s + b \log M_s + c \log T_X = \text{const.}$, with $a = 0.71^{+0.06}_{-0.10}$, $b = -0.53^{+0.02}_{-0.01}$, and $c = 0.46^{+0.13}_{-0.11}$. The values of (a, b, c) are consistent with those for the CLASH sample within the errors (Table 1). The thickness of the plane or the dispersion in the direction of P_3 is $0.039^{+0.021}_{-0.010}$, which is slightly smaller than, but consistent within the errors with the CLASH result (Paper I). Here we note that lensing measurements are sensitive to projection effects, and NFW fitting based on the assumption of spherical symmetry can introduce a sizable scatter in the derived mass and concentration parameters, or (r_s, M_s). In our error analysis of the CLASH lensing data (Umetsu et al. 2016), we properly accounted for the projection effects due to cluster halo triaxiality and uncorrelated large-scale structure projected along the line of sight (Gruen et al. 2015), implying that the thickness of the FP derived from our CLASH data should not be affected by the external scatter introduced by the lensing projection effects. The X-ray sample has a wider range of r_s and M_s compared with the CLASH sample (Figure 1 in Paper I). Since the errors of a, b, and c are not independent of each other, we show in Figure 4 the likelihood contours of the parameters describing the direction of the plane normal P_3 for the X-ray sample (black solid lines). In that figure, θ is the angle between P_3 and the $\log T_X$ axis, and ϕ is the azimuthal angle around the $\log T_X$ axis, measured anti-clockwise from the $\log r_s$ axis, or $\tan\phi = b/a$ (Table 1). The contours are elongated in the direction of rotation around P_1 (Figure 3(a)), to which the direction P_3 is less constrained. The contours show that the direction of P_3 is consistent with that for the CLASH sample (red dotted lines; see Paper I). As long as clusters are widely distributed on the plane, the direction of P_3 should not be too affected by a possible sample selection bias. In Figure 4, we also plotted MUSIC simulation results (see Paper I for details) and the prediction of the similarity solution (SSol), which is given by Equation (4) with $n = -2$ and -2.5. They are the same as those in Figure 2 of Paper I and are consistent with the X-ray data at the $\sim 1\sigma$ level. For the virial expectation, the angle θ is the one between vectors $(1/\sqrt{3}, -1/\sqrt{3}, 1/\sqrt{3})$ and $(0, 0, 1)$, which is $\approx 55°$. The prediction of the virial expectation is rejected at the 99% confidence level.

In Paper I, using the results of numerical simulation, we showed that the plane parameters are not very dependent on the

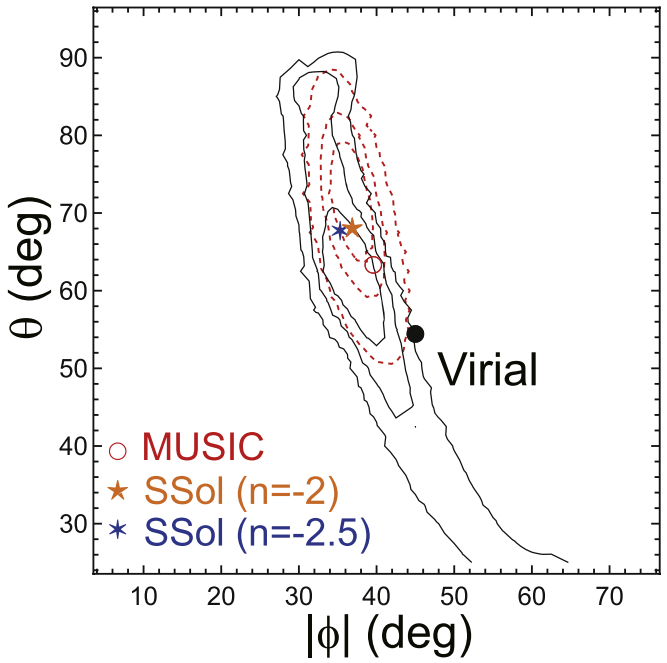

Figure 4. Direction of the plane normal $P_3 = (a, b, c)$ in the space of ($\log r_s$, $\log M_s$, $\log T_X$). Probability contours for the sample of 44 X-ray clusters (black solid lines) are shown at the 68% (1σ), 90%, and 99% confidence levels from inside to outside. The prediction of the virial expectation ($r_s M_s^{-1} T_X \propto$ const) corresponds to (ϕ, θ) = ($-45°$, $55°$) (black dot), and is rejected at the 99% confidence level. Probability contours for the CLASH sample (red dotted lines; see Figure 2 of Paper I) are shown for comparison. The plane normal derived for the MUSIC simulation sample is shown by the open red circle; it is located around the 68% contour level and consistent with the X-ray observations at that level. Predictions based on a similarity solution (SSol) for $n = -2$ and $n = -2.5$ are shown by the orange and blue stars, respectively.

relaxation state of clusters, although irregular clusters tend to slightly increase the scatter of the FP. That is, although the cluster parameters (r_s, M_s, T_X) can fluctuate substantially, especially during major mergers, the particular combination of these parameters that determines the FP (e.g., the left side of Equation (4)) can remain nearly constant. As a result, clusters evolve along the FP and do not much deviate from the FP even during a cluster merger (Section 5.2 in Paper I). Here, we study this issue using the X-ray sample. Ettori et al. (2010) classified the X-ray sample into 18 cool-core (CC) clusters, 19 non-cool-core (NCC) clusters, and 7 intermediate cool-core (ICC) clusters based on the entropy of the ICM in the central region. The CC and NCC clusters tend to be regular and irregular in shape, respectively. We performed the FP analysis for the CC and ICC+NCC samples separately and the results are shown in Table 1. The plane directions are not much different from that of the whole sample of 44 clusters. The thickness of the plane is $0.026^{+0.014}_{-0.006}$ for CC and $0.043^{+0.019}_{-0.010}$ for ICC+NCC, which can be compared with the one for the whole sample ($0.039^{+0.021}_{-0.010}$). Since r_s is generally much larger than the cluster core, the details of the ICM physics in the core region are not expected to significantly affect the global cluster parameters, ($\log r_s$, $\log M_s$, $\log T_X$). Although the thicknesses of the planes for the different subsamples are consistent with each other within errors, CC (ICC+NCC) clusters may give a smaller (larger) dispersion about the plane. We note that while the size of the ICC sample alone is too small to reliably determine their

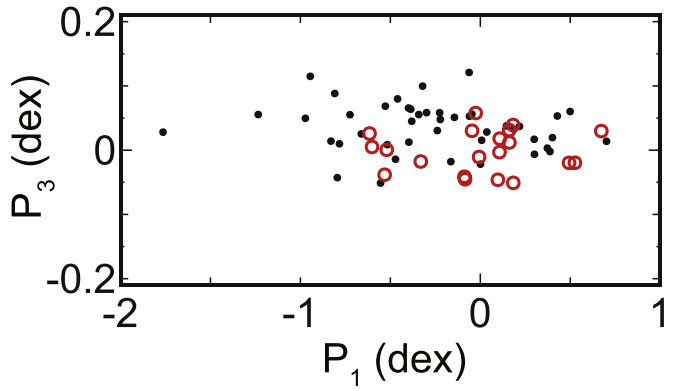

Figure 5. Cross section of the CFP (red circles) and the XFP (black dots). The coordinates P_1 and P_3 are for the CFP.

FP parameters, the thickness of the plane is slightly increased by including the ICC sample compared to the NCC-only case.

5. Shift of the Planes and Mass Calibration

Figure 5 shows the cross sections of the FPs for the CLASH and X-ray samples depicted on the same plane coordinate. Although they overlap with each other, the FP for the CLASH sample (CFP) is located slightly above the FP for the X-ray sample (XFP). Fixing the angles of both planes to the same one given by Equation (4) with $n = -2$ (SSol in Table 1), we estimate the distance between the two FPs and find that it is $d_{\rm FP} = 0.031^{+0.027}_{-0.039}$ dex in the space of ($\log r_s$, $\log M_s$, $\log T_X$). Thus, the shift of the two planes is not significant. The error of the distance mostly comes from the observational errors of the X-ray data, which result in the uncertainty of the position of the XFP.

However, X-ray data will be enriched and the configuration of the FP could be determined much more precisely in the near future. In principle, the FP can be used as a benchmark of data calibration, because numerical simulations have shown that the FP is very thin and its origin has been explained by the similarity solution (Paper I). Here, we demonstrate that a possible shift of the FP could be used to calibrate cluster masses M_Δ obtained with X-ray observations. It would be useful even for studies of cluster number counts based on masses estimated by the Sunyaev–Zel'dovich effect, because this estimation relies on X-ray data for calibration (Planck Collaboration et al. 2014). In the following, we use the current observational data sets, although they may not be accurate enough for our calibration purposes.

We study the shift of the XFP against the CFP assuming that the shift is caused by some observational systematic errors. Given the fairly large statistical uncertainties, and for the sake of simplicity, the angles of both FPs are fixed (SSol for $n = -2$ in Table 1), because the direction is consistent with both the CFP and XFP (Figure 4) and the distance between two planes can be well defined only when the planes are parallel. If the data quality and size are improved in the future, this constraint may not be needed. Since both FPs use X-ray data for the temperature, and since the temperature has been corrected by Equation (12), we assume that there is no systematic error for temperature, for simplicity. In that case, the shift of the planes may be attributed to the systematic error of M_s and/or r_s. The errors of M_s and r_s may come from the assumption of hydrostatic equilibrium and the limited radial range adopted in X-ray analysis, respectively (e.g., Nagai et al. 2007; Rasia

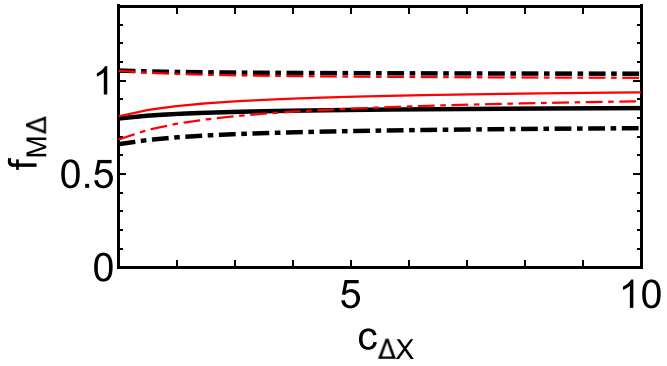

Figure 6. Relation between $f_{M\Delta}$ and $c_{\Delta X}$. The thick black lines are derived from Equation (15) and the thin red lines are derived from Equation (17). The solid lines are for the most certain values of f_{Ms} (thick black) or f_{rs} (thin red). The dashed–dotted lines show the uncertainties attributed to those of f_{Ms} (thick black) or f_{rs} (thin red).

et al. 2013). First, let us assume that the XFP is shifted solely in the direction of M_s. In this case, the positions of a given cluster on the CFP and the XFP are given by (r_s, M_{sC}, T_X) and (r_s, M_{sX}, T_X), respectively. From now on, we shall use subscript C or X if the value is specifically related to the CFP or the XFP, respectively. Since the two FPs are parallel, the ratio $f_{Ms} \equiv M_{sX}/M_{sC}$ is not unity but is independent of clusters. However, the ratio of M_Δ among the two FPs or $f_{M\Delta} \equiv M_{\Delta X}/M_{\Delta C}$ can vary because M_Δ is a function of c_Δ (Equation (9)) that is not constant among clusters. In the Appendix, we show that $f_{M\Delta}$ is represented by a function of $c_{\Delta X}$ (Equation (15)) or $c_{\Delta C}$ (Equation(16)) for a given f_{Ms}. Second, let us assume that the XFP is shifted solely in the direction of r_s. In this case, the positions of a given cluster on the CFP and the XFP are given by (r_{sC}, M_s, T_X) and (r_{sX}, M_s, T_X), respectively. The ratio $f_{rs} \equiv r_{sX}/r_{sC}$ is not unity but is independent of clusters. For the second case, we can also derive $f_{M\Delta}$ as a function of $c_{\Delta X}$ (Equation (17)) or $c_{\Delta C}$ (Equation (18)) for a given f_{rs}.

Figure 6 shows the relation between $f_{M\Delta}$ and $c_{\Delta X}$ for our CLASH and X-ray samples. The results do not depend on the value of Δ. Since we assumed that the normal of the two FPs is given by Equation (4) for $n = -2$, it is written as $P_3 = (a, b, c) = (0.74, -0.56, 0.37)$ (SSol in Table 1). If the shift of the FP is caused by a systematic error of M_s, we have $f_{Ms} = 10^{d_{\rm FP}/b} = 0.88^{+0.15}_{-0.09}$. Thus, $f_{M\Delta}$ can be derived from Equation (15), which is shown by the thick black lines in Figure 6. On the other hand, if the shift of the FP is caused by a systematic error of r_s, we have $f_{rs} = 10^{d_{\rm FP}/a} = 1.10^{+0.10}_{-0.12}$. Thus, $f_{M\Delta}$ is derived from Equation (17), which is shown by the thin red lines in Figure 6. The f_{Ms}–$c_{\Delta C}$ relation is almost the same as the f_{Ms}–$c_{\Delta X}$ relation.

Figure 6 shows that $f_{M\Delta}$ does not much depend on $c_{\Delta X}$ and the dependence can be ignored. given the accuracy of the current observations. The dashed–dotted lines suggest that the uncertainty caused by the error of f_{Ms} (black dashed–dotted lines) is larger than that caused by the error of f_{rs} (red dashed–dotted lines). The actual uncertainty should be between the two. If we conservatively adopt the former, $f_{M\Delta} = M_{\Delta X}/M_{\Delta C} \sim 0.85^{+0.2}_{-0.2}$, which means that the mass estimated from the X-ray data may be systematically underestimated compared with that estimated from the CLASH data, but the evidence is not solid. The value of $f_{M\Delta}$ we obtained is consistent with that predicted by numerical simulations (Nagai et al. 2007; Piffaretti & Valdarnini 2008; Laganá et al. 2010; Rasia et al. 2012). Future improvements of observational data, especially X-ray data, are desired to make a firm conclusion. For the analysis of those data, the dependence of $f_{M\Delta}$ on c_Δ will need to be taken into account. The direction of the plane shift could be determined if the r_s and M_s of certain clusters were precisely determined from both X-ray and gravitational lensing observations. Mock observations of simulated clusters would also be useful to study the shift. Possible differences in the angles of the CFP and the XFP could be a clue for identifying the origin of the observational systematic errors. It would also be interesting to compare the XFPs obtained with different instruments (e.g., *Chandra* and *XMM-Newton*) for calibration including T_X.

6. Summary

We have investigated the origin of the mass–temperature relation of galaxy clusters. Observations and numerical simulations have shown that the relation is approximately represented by $M_\Delta \propto T_X^{3/2}$ (e.g., $\Delta = 500$). This relation has been interpreted as evidence that clusters are in virial equilibrium within r_Δ. However, the existence of the FP of clusters and its interpretation based on the modern inside-out scenario suggest that clusters are not in virial equilibrium in the whole region within r_Δ and that the temperatures of clusters are primarily determined by the characteristic mass M_s and radius r_s of the NFW profile, rather than M_Δ. We have solved this discrepancy by combining the FP with the concentration–mass–redshift relation of cluster halos calibrated by N-body simulations. The relation $M_\Delta \propto T_X^{3/2}$ is derived from the FP relation among r_s, M_s, and T_X using the mass dependence of c_Δ. We also showed that the dispersion of the c_Δ–M_Δ relation can largely account for the spread of the cluster distribution on the FP. Moreover, we confirmed that the FP constructed from X-ray data alone is consistent with that from gravitational lensing data. The FP could be used to calibrate the cluster parameters derived with different methods. As an example, we demonstrated that a cluster mass derived from X-ray observations is systematically $\sim 85^{+20}_{-20}\%$ of that derived from gravitational lensing observations.

We thank the anonymous referee, whose comments greatly improved the clarity of this paper. This work was supported by MEXT KAKENHI No. 15K05080 (Y.F.). K.U. acknowledges support from the Ministry of Science and Technology of Taiwan (grant MOST 106-2628-M-001-003-MY3) and from the Academia Sinica Investigator Award. S.E. acknowledges financial contribution from the contracts NARO15 ASI-INAF I/037/12/0, ASI 2015-046-R.0 and ASI-INAF n.2017-14-H.0. E.R. acknowledges support from the ExaNeSt and EuroExa projects, funded by the European Unions Horizon 2020 research and innovation program under grant agreements No. 671553 and No. 754337, respectively.

Appendix
The Mass Ratio between the FP

First, we assume that the XFP is shifted from the CFP solely in the direction of M_s. From Equation (5),

$$M_s = 4\pi\delta_c\rho_c r_s^3(\ln 2 - 1/2). \quad (13)$$

Thus, the ratio f_{Ms} is equivalent to that of δ_c among the XFP and the CFP or δ_{cX}/δ_{cC} if r_s does not depend on the FPs. If we define $\delta'_c \equiv \delta_c/\Delta$, we have $f_{Ms} = \delta'_{cX}/\delta'_{cC}$. From Equations (7) and (8), the inverse function of δ'_c can be defined, which we call $\tilde{c}_\Delta(\delta'_c)$. From Equations (6) and (3),

$$f_{M\Delta} = \frac{M_{\Delta X}}{M_{\Delta C}} = \left(\frac{r_{\Delta X}}{r_{\Delta C}}\right)^3 = \left(\frac{c_{\Delta X}}{c_{\Delta C}}\right)^3 = \left(\frac{c_{\Delta X}}{\tilde{c}_\Delta(\delta'_{cC})}\right)^3 = \left(\frac{c_{\Delta X}}{\tilde{c}_\Delta(f_{Ms}^{-1}\delta'_{cX})}\right)^3 \quad (14)$$

Since $\delta'_{cX} = y(c_{\Delta X})$ from Equations (7) and (8), we obtain

$$f_{M\Delta} = \left(\frac{c_{\Delta X}}{\tilde{c}_\Delta(f_{Ms}^{-1} y(c_{\Delta X}))}\right)^3, \quad (15)$$

which is a function of $c_{\Delta X}$ for a given f_{Ms}. It can also be written as

$$f_{M\Delta} = \left(\frac{\tilde{c}_\Delta(f_{Ms}\delta'_{cC})}{c_{\Delta C}}\right)^3 = \left(\frac{\tilde{c}_\Delta(f_{Ms} y(c_{\Delta C}))}{c_{\Delta C}}\right)^3, \quad (16)$$

and it is a function of $c_{\Delta C}$ for a given f_{Ms}.

Second, we assume that the XFP is shifted from the CFP solely in the direction of r_s. From Equation (13), we obtain $\delta'_{cC}/\delta'_{cX} = \delta_{cC}/\delta_{cX} = (r_{sX}/r_{sC})^3 = f_{rs}^3$ if M_s does not depend on the FPs. From Equations (6) and (3),

$$f_{M\Delta} = \left(\frac{r_{\Delta X}}{r_{\Delta C}}\right)^3 = \left(\frac{c_{\Delta X} r_{sX}}{c_{\Delta C} r_{sC}}\right)^3 = f_{rs}^3\left(\frac{c_{\Delta X}}{\tilde{c}_\Delta(\delta'_{cC})}\right)^3 = f_{rs}^3\left(\frac{c_{\Delta X}}{\tilde{c}_\Delta(f_{rs}^3\delta'_{cX})}\right)^3 = f_{rs}^3\left(\frac{c_{\Delta X}}{\tilde{c}_\Delta(f_{rs}^3 y(c_{\Delta X}))}\right)^3, \quad (17)$$

which is a function of $c_{\Delta X}$ for a given f_{rs}. Similarly, we have

$$f_{M\Delta} = f_{rs}^3\left(\frac{\tilde{c}_\Delta(f_{rs}^{-3}\delta'_{cC})}{c_{\Delta C}}\right)^3 = f_{rs}^3\left(\frac{\tilde{c}_\Delta(f_{rs}^{-3} y(c_{\Delta C}))}{c_{\Delta C}}\right)^3, \quad (18)$$

and it is a function of $c_{\Delta C}$ for a given f_{rs}.

ORCID iDs

Yutaka Fujita https://orcid.org/0000-0003-0058-9719
Keiichi Umetsu https://orcid.org/0000-0002-7196-4822
Elena Rasia https://orcid.org/0000-0003-4175-002X
Nobuhiro Okabe https://orcid.org/0000-0003-2898-0728
Massimo Meneghetti https://orcid.org/0000-0003-1225-7084

References

Bahcall, N. A., & Cen, R. 1993, ApJL, 407, L49
Bertschinger, E. 1985, ApJS, 58, 39
Bhattacharya, S., Habib, S., Heitmann, K., & Vikhlinin, A. 2013, ApJ, 766, 32
Borgani, S., & Kravtsov, A. 2011, ASL, 4, 204
Bryan, G. L., & Norman, M. L. 1998, ApJ, 495, 80
Bullock, J. S., Kolatt, T. S., Sigad, Y., et al. 2001, MNRAS, 321, 559
Correa, C. A., Wyithe, J. S. B., Schaye, J., & Duffy, A. R. 2015, MNRAS, 452, 1217
Diemer, B., & Kravtsov, A. V. 2015, ApJ, 799, 108
Donahue, M., Voit, G. M., Mahdavi, A., et al. 2014, ApJ, 794, 136
Duffy, A. R., Schaye, J., Kay, S. T., & Dalla Vecchia, C. 2008, MNRAS, 390, L64
Dutton, A. A., & Macciò, A. V. 2014, MNRAS, 441, 3359
Eisenstein, D. J., & Hu, W. 1998, ApJ, 496, 605
Eke, V. R., Cole, S., & Frenk, C. S. 1996, MNRAS, 282, 263
Ettori, S., De Grandi, S., & Molendi, S. 2002, A&A, 391, 841
Ettori, S., & Fabian, A. C. 1999, MNRAS, 305, 834
Ettori, S., Gastaldello, F., Leccardi, A., et al. 2010, A&A, 524, A68
Finoguenov, A., Reiprich, T. H., & Böhringer, H. 2001, A&A, 368, 749
Fujita, Y., & Takahara, F. 1999, ApJL, 519, L55
Fujita, Y., Umetsu, K., Rasia, E., et al. 2018, ApJ, 857, 118
Gruen, D., Seitz, S., Becker, M. R., Friedrich, O., & Mana, A. 2015, MNRAS, 449, 4264
Israel, H., Schellenberger, G., Nevalainen, J., Massey, R., & Reiprich, T. H. 2015, MNRAS, 448, 814
Kaiser, N. 1986, MNRAS, 222, 323
Laganá, T. F., de Souza, R. S., & Keller, G. R. 2010, A&A, 510, A76
Lieu, M., Smith, G. P., Giles, P. A., et al. 2016, A&A, 592, A4
Ludlow, A. D., Navarro, J. F., Boylan-Kolchin, M., et al. 2013, MNRAS, 432, 1103
Meneghetti, M., Rasia, E., Vega, J., et al. 2014, ApJ, 797, 34
Nagai, D., Vikhlinin, A., & Kravtsov, A. V. 2007, ApJ, 655, 98
Navarro, J. F., Frenk, C. S., & White, S. D. M. 1997, ApJ, 490, 493
Neumann, D. M., & Arnaud, M. 1999, A&A, 348, 711
Nevalainen, J., David, L., & Guainazzi, M. 2010, A&A, 523, A22
Nevalainen, J., Markevitch, M., & Forman, W. 2000, ApJ, 532, 694
Piffaretti, R., & Valdarnini, R. 2008, A&A, 491, 71
Planck Collaboration, Ade, P. A. R., Aghanim, N., et al. 2014, A&A, 571, A20
Planelles, S., Schleicher, D. R. G., & Bykov, A. M. 2015, SSRv, 188, 93
Postman, M., Coe, D., Benítez, N., et al. 2012, ApJS, 199, 25
Rasia, E., Borgani, S., Ettori, S., Mazzotta, P., & Meneghetti, M. 2013, ApJ, 776, 39
Rasia, E., Meneghetti, M., Martino, R., et al. 2012, NJPh, 14, 055018
Reiprich, T. H., & Böhringer, H. 2002, ApJ, 567, 716
Salvador-Solé, E., Solanes, J. M., & Manrique, A. 1998, ApJ, 499, 542
Schellenberger, G., Reiprich, T. H., Lovisari, L., Nevalainen, J., & David, L. 2015, A&A, 575, A30
Shi, X. 2016a, MNRAS, 459, 3711
Shi, X. 2016b, MNRAS, 461, 1804
Sun, M., Voit, G. M., Donahue, M., et al. 2009, ApJ, 693, 1142
Truong, N., Rasia, E., Mazzotta, P., et al. 2018, MNRAS, 474, 4089
Umetsu, K., Zitrin, A., Gruen, D., et al. 2016, ApJ, 821, 116
Vikhlinin, A., Kravtsov, A., Forman, W., et al. 2006, ApJ, 640, 691
Vikhlinin, A., Kravtsov, A. V., Burenin, R. A., et al. 2009, ApJ, 692, 1060
Wechsler, R. H., Bullock, J. S., Primack, J. R., Kravtsov, A. V., & Dekel, A. 2002, ApJ, 568, 52
Xu, H., Jin, G., & Wu, X.-P. 2001, ApJ, 553, 78
Zhao, D. H., Jing, Y. P., Mo, H. J., & Börner, G. 2009, ApJ, 707, 354
Zhao, D. H., Mo, H. J., Jing, Y. P., & Börner, G. 2003, MNRAS, 339, 12
Zhao, H.-H., Li, C.-K., Chen, Y., Jia, S.-M., & Song, L.-M. 2015, ApJ, 799, 47